Comput. Methods Appl. Mech. Engrg. 198 (2009) 3567–3582

Contents lists available at ScienceDirect

Comput. Methods Appl. Mech. Engrg.

journal homepage: www.elsevier.com/locate/cma

Simulation of intracranial aneurysm stenting: Techniques and challenges

Sunil Appanaboyina [a], Fernando Mut [a], Rainald Löhner [a], Christopher Putman [b], Juan Cebral [a,*]

[a] Center for Computational Fluid Dynamics, George Mason University, 4400 University Drive, MSN 6A2, Fairfax, VA 22030, USA
[b] Interventional Neuroradiology, Inova Fairfax Hospital, 3300 Gallows Road, Falls Church, VA 22042, USA

ARTICLE INFO

Article history:
Received 30 December 2007
Received in revised form 3 January 2009
Accepted 20 January 2009
Available online 31 January 2009

Keywords:
Cerebral aneurysms
Computational fluid dynamics
Stenting
Adaptive embedded unstructured grids
Hemodynamics

ABSTRACT

Recently, there has been considerable interest in the use of stents as endovascular flow diverters for the treatment of intracranial aneurysms. Simulating this novel method of treatment is essential for understanding the intra-aneurysmal hemodynamics in order to design better stents and to personalize and optimize the endovascular stenting procedures. This paper describes a methodology based on unstructured embedded grids for patient-specific modeling of stented cerebral aneurysms, demonstrates how the methodology can be used to address specific clinical questions, and discusses remaining technical issues. In particular, simulations are presented on a number of patient-specific models constructed from medical images and using different stent designs and treatment alternatives. Preliminary sensitivity analyses with respect to stent positioning and truncation of the stent model are presented. The results show that these simulations provide useful and valuable information that can be used during the planning phase of endovascular stenting interventions for the treatment of intracranial aneurysms.

1. Introduction

Stroke is the leading cause of long-term disabilities and the third cause of death after heart attack and cancer in the western word [1–7]. It consists in the death of part of the brain due to oxygen deficiency. There are two types of strokes, ischemic stroke and subarachnoid hemorrhage (SAH). The former is caused by diminution of cerebral blood flow below certain threshold and the latter due to bleeding into the intracranial space. About 80% of SAH are caused by the rupture of cerebral aneurysms. A cerebral/intracranial aneurysm is a cerebrovascular disorder in which an abnormal balloon like dilation grows on the wall of a cerebral artery. These aneurysms commonly occur at the base of the brain in the so-called the arterial Circle of Willis. The exact reason for the genesis of these aneurysms is not well understood. Research shows that different factors such as genetics, hemodynamics and wall biomechanics play important roles [31]. In addition, hemodynamic features such as wall shear stress, jetting, and vorticity are thought to play a fundamental role in the growth and ultimately the rupture of the aneurysm. Due to the life-threatening effects of SAH, when physicians identify an unruptured aneurysm, they often consider preventive treatment. Surgical clipping and coil embolization are the most common methods of treatment [8]. Surgical clipping involves placing a metallic clip across the neck of the aneurysm thereby blocking the blood from entering into the aneurysm. Endovascular embolization is a minimally invasive technique that consists in packing the aneurysm with platinum coils. The idea here is to clot the blood inside the aneurysm and completely stop the intra-aneurysmal flow. Both procedures intend to isolate the aneurysm from the arterial circulation thus preventing aneurysm rupture and hence the hemorrhage. Surgical clipping is not always the favoured choice due to the high risks involved with craniotomy and the impossibility of clipping certain aneurysms due to their location and shape. Endovascular embolization also has some serious complications. Numerous cases of coil compaction leading to the re-growth or the formation of a secondary aneurysm have been reported. Moreover, wide neck or fusiform aneurysm cannot be treated with coils alone. In cases like these a stent – an expandable metallic mesh – is deployed in the parent vessel to hold the coils inside the aneurysm dome.

Recently, there has been growing interest in the use of stents as flow diverters without coils. The goal of this treatment is to disrupt the inflow to the aneurysm and cause a complete thrombosis of the aneurysm [9–11]. This requires new stents specifically designed to achieve this goal.

Numerous studies have been published concerning the aneurysmal flow alterations caused by stents alone using idealized in vitro and numerical models [12–15]. Although these studies have provided valuable information about the fluid dynamic behavior of these stents, the results from these studies cannot be generalized in a straightforward manner to the patient population or used to plan the endovascular treatment of individual aneurysms. Therefore, personalized or patient-specific models have also been used to better understand the interaction between the stent and the complex swirling flows in realistic anatomies

* Corresponding author. Tel.: +1 703 993 4078; fax: +1 703 993 9300.
E-mail address: jcebral@gmu.edu (J. Cebral).

0045-7825/$ - see front matter © 2009 Elsevier B.V. All rights reserved.
doi:10.1016/j.cma.2009.01.017

[16–19,24,29,26,25,28]. These studies have shown that stents can produce significant alterations in the intra-aneurysmal blood flow patterns, but it is still not clear whether these alterations will cause complete occlusion of the aneurysm and thus be a viable durable treatment. It has also been pointed out that in some cases, the implantation of stent can produce adverse hemodynamic conditions [26]. Therefore, further studies of the hemodynamic alterations produced by stents and treatment outcomes need to be carried out.

However, simulating blood flow past endovascular devices such as stents in patient-specific models poses a number of challenges [30]. These include: techniques for virtual deployment of stents, meshing the vascular model and the deployed stent [32,33], developing appropriate pre- and post-stenting boundary conditions, and handling of relatively large computational meshes. This paper addresses some of these technical issues using an unstructured grid embedding approach and discusses different clinical questions that can be investigated with these simulations. The aim is to point out the major challenges and provide guide to new investigators conducting research in aneurysm flow diversion using patient-specific image-based computational models.

2. Methods

The methodology for image-based simulation of blood flows in stented cerebral aneurysms can be divided into the following stages: (1) vascular modeling, (2) stent deployment, (3) meshing, (4) hemodynamics modeling, and (5) data reduction and visualization.

2.1. Vascular modeling

Patient-specific models of cerebral aneurysms and the connected vessels are created from 3D rotational angiography (3DRA) images using a previously developed method [19,20]. Briefly, this method consists of the following operations. To reduce the noise in the image it is first filtered briefly using a combination of blurring and sharpening operations. The image is then segmented using the seeded region growing algorithm. Using an advancing tetrahedra algorithm an initial model of the image is obtained by iso-surface extraction. This extracted iso-surface is then allowed to deform under the action of internal smoothing forces and external forces obtained from the gradients of the original un-processed image [21]. The deformable model makes the surface coincide with the vessel boundaries detected in the image. The surface is then smoothed using a non-shrinking algorithm [22] and the vessels are interactively truncated perpendicularly to their axis. If desired the boundaries are extruded in order to minimize the influence of the boundary conditions in the region of interest. While the segmentation step aims at reconstructing the correct vascular topology, the geometrical modeling step aims at accurately representing the vascular geometry. Both the correct topology and geometry of the aneurysm and parent vessel are required for an accurate representation of the in vivo hemodynamics. The geometrical model is then used to generate a finite element mesh composed of tetrahedral elements using an advancing front method. The surface of the model is re-triangulated and this mesh marches inwards filling the volume with tetrahedra elements [35,36]. In order to resolve all the flow features in the flow simulation, the size of the element is chosen in such a way that every vessel has at least a given minimum number of elements across the diameter. Such discretizations are created using an adaptive background grid that defines the spatial variation of element size in space. Typically, meshes with a minimum resolution of 0.02 cm are used resulting in pre-stent grids with approximately 2–5 million elements. This methodology was used to construct patient-specific models of four aneurysms in the internal carotid artery near the ophthalmic artery, two aneurysms at the tip of the basilar artery and one model of a patient with an aneurysm in the anterior communicating artery and another two in the left middle cerebral artery. These models were used to study the effect of different stenting options.

2.2. Stent deployment

The stent deployment methodology consist in the following steps: (a) extraction of the vessel centerline, (b) deformation of a cylindrical support surface along the vessel skeleton until it conforms to the vessel walls, and (c) mapping of stent designs using the deformed support surface. The skeleton of the parent vessel is extracted from the vascular model using a previously developed algorithm [43]. A cylindrical support surface is then generated along this skeleton. Assuming this surface to be elastic it is deformed under the influence of internal smoothing forces and external attractive forces to the vessel wall. The external forces consist of an inflating or radial force proportional to the distance vector between points in the triangulated surface and the centerline. The internal smoothing forces are based on the classical Laplacian smoothing operator. These are basically attractive forces between each point in the triangulated surface and its first neighbors. The positions of the vertices of the cylindrical surface are updated using a classical Newtonian law of motion:

$$m_i \frac{\partial^2 \mathbf{p}_i}{\partial t^2} + \gamma \frac{\partial \mathbf{p}_i}{\partial t} - \tilde{\alpha}_i f_{int}(\mathbf{p}_i) = \tilde{\beta}_i f_{ext}(\mathbf{p}_i), \tag{1}$$

where $\mathbf{p}_i$ is the position vector of point i, m_i is the ith vertex mass, γ is a damping parameter, and f_{int} and f_{ext} represent the internal and external forces, respectively. The parameters $\tilde{\alpha}_i$ and $\tilde{\beta}_i$ controls the influence of the internal and external forces, respectively. The discretization of Eq. (1) using a fully explicit discretization scheme leads to [34]

$$\mathbf{p}_i^{n+1} = \mathbf{p}_i^n + (1-\gamma)(\mathbf{p}_i^n - \mathbf{p}_i^{n-1}) + \alpha_i f_{int}(\mathbf{p}_i^n) + \beta_i f_{ext}(\mathbf{p}_i^n), \tag{2}$$

where α_i and β_i are force weights including the point mass and the timestep. Stability of this scheme depends on α_i, β_i, and γ lying inside $[0,1/2]$, $[0,1]$, and $[0,1]$, respectively. All the cases in this text were performed with the parameters $\gamma = 1$, $\alpha_i = 0.01$, and $\beta_i = 0.0005$. These values were selected on a trial and error basis using several test cases. In the initial stage the cylindrical surface which is made up of shell elements is at the center of the parent vessel. As time progresses a combination of f_{int} and f_{ext} are used to pull the cylinder towards the vessel walls. This deformation process is interactively stopped when most of the points on the cylindrical surface are on the vessel wall. During the deformation process if a point on the cylindrical surface crossed the vessel wall its normal distance changes sign, then it is projected back to the vessel wall and fixed. Once the final cylindrical surface is obtained then different stent designs can be mapped onto it. The stent design is drawn as a collection of connected lines on a rectangular region with the same dimensions as the undeformed cylindrical support surface. This rectangular region is triangulated and the local coordinates of the points defining the stent design are calculated. The same local coordinates of these points but on the deformed triangulation are then used to obtain the deformed or deployed stent design. The deformed design is then used to generate beads of overlapping spheres with the appropriate thickness along the lines and mapped onto the surface of the deformed cylinder in order to obtain the final stent model in the deployed state. In order to illustrate the methodology, three stent designs were considered: (a) a Neuroform stent, (b) a left rotating helical stent, and (c) a right rotating helical stent. All these stents had the same wire diameter (0.01 cm) and roughly the same porosity.

2.3. Meshing

The traditional computational mesh which is generated in order to simulate the flow of blood inside the parent vessel and in the presence of a stent is called a body-conforming mesh. Traditionally, body-conforming grids have been used to simulate blood flows in vascular models. However, the main difficulty in generating such a mesh for stented aneurysms is that it requires a watertight assembly of analytical and/or discrete surface patches to describe the surface of the computational domain. Past experience has shown that the creation of such a watertight geometrical model can be tedious and challenging even for simple vascular geometries [27]. In contrast, unstructured embedded grid approaches provide an effective automatic way of performing patient-specific blood flow simulations in the presence of stents. In this approach a body-fitted unstructured grid is created for the vascular model and the stent is embedded into this mesh [33]. The elements of the mesh that are cut by the surface of the stent are identified and adaptively refined in order to increase the resolution of the mesh around the stent wires. The edges of the final mesh that are cut by the stent are excluded from the flow calculation and no-slip boundary conditions are imposed at the cut-points. The geometry of the stent can be represented either as a surface triangulation (explicit surface definition) or by a series of overlapping spheres (implicit surface definition) [28]. In the latter approach, the distance between the spheres can be adjusted to represent the stent to any degree of accuracy. In the embedded technique, since the geometry of the stent is only used to determine the elements cut by the stent in the computational grid, these two approaches differ only in the way that the intersection between the stent wire surface and the computational grid is computed. In the former approach this means computing the intersection between triangles of the stent surface and edges of the computational tetrahedral mesh. Whereas, in the latter approach its the intersection between the edges and the spheres. The latter one is easier to implement.

2.4. Hemodynamic modeling

Blood has been typically considered a Newtonian incompressible fluid. It has been shown that blood behaves as a Newtonian fluid in large arteries [23]. Also, hemodynamic analyses of cerebral aneurysm models with realistic anatomies using Newtonian and non-Newtonian approximations have indicated that the main flow characteristics are not significantly affected by the viscosity model [20]. However, non-Newtonian effects can become important in the slow flows encountered in stented aneurysms. This issue deserves further investigation. Based on these assumptions, the governing equations are the unsteady Navier–Stokes equations in three dimensions [37]:

$$\nabla \cdot v = 0, \tag{3}$$

$$\frac{\partial v}{\partial t} + v \cdot \nabla v = -\frac{1}{\rho}\nabla p + \nu \nabla^2 v, \tag{4}$$

where v is velocity, p is pressure, ρ is density, and ν is kinematic viscosity. In the simulations, values of ρ = 1.0 gr/cm^3 and ν = 0.04 cm^2/s were used. These equations are discretized in time using an implicit scheme of the form:

$$\nabla \cdot v^{n+\theta} = 0, \tag{5}$$

$$\frac{v^{n+\theta} - v^n}{\theta \Delta t} + v^{n+\theta} \cdot \nabla v^{n+\theta} + \frac{1}{\rho}\nabla p^{n+\theta} = \nabla v \cdot \nabla v^{n+\theta}. \tag{6}$$

The parameter θ selects the time integration scheme used in the simulation. If $\theta = 1$ the first order backward Euler scheme is recovered while with $\theta = 1/2$ the second order Crank–Nicholson is obtained. Moving the first term to the right-hand side, this scheme can be interpreted as the steady-state solution of the pseudo-time system:

$$\frac{\partial v^{n+\theta}}{\partial \tau} + v^{n+\theta} \cdot \nabla v^{n+\theta} + \frac{1}{\rho}\nabla p^{n+\theta} = \nabla v \cdot \nabla v^{n+\theta} - \frac{v^{n+\theta} - v^n}{\theta \Delta t}. \tag{7}$$

This is similar to the original Navier–Stokes equation but with a source term on the right-hand side. The solution is then advanced in time by solving a steady-state problem in pseudo-time τ at each timestep. A linear (tetrahedral) finite element discretization of space is used. The discrete system is obtained via the Galerkin weighted residual method. An edge-based formulation is used for efficiency. The resulting discrete system is of the form:

$$K^{ij}\Delta u^j = \sum_{ij_\Omega} C^{ij}(F_i + F_j), \tag{8}$$

where K^{ij}, C^{ij}, F_i, Δu^i denote the implicit left-hand side matrix, the explicit right-hand side matrix entries, nodal fluxes and increments in the nodal unknowns. The numerical scheme becomes unstable

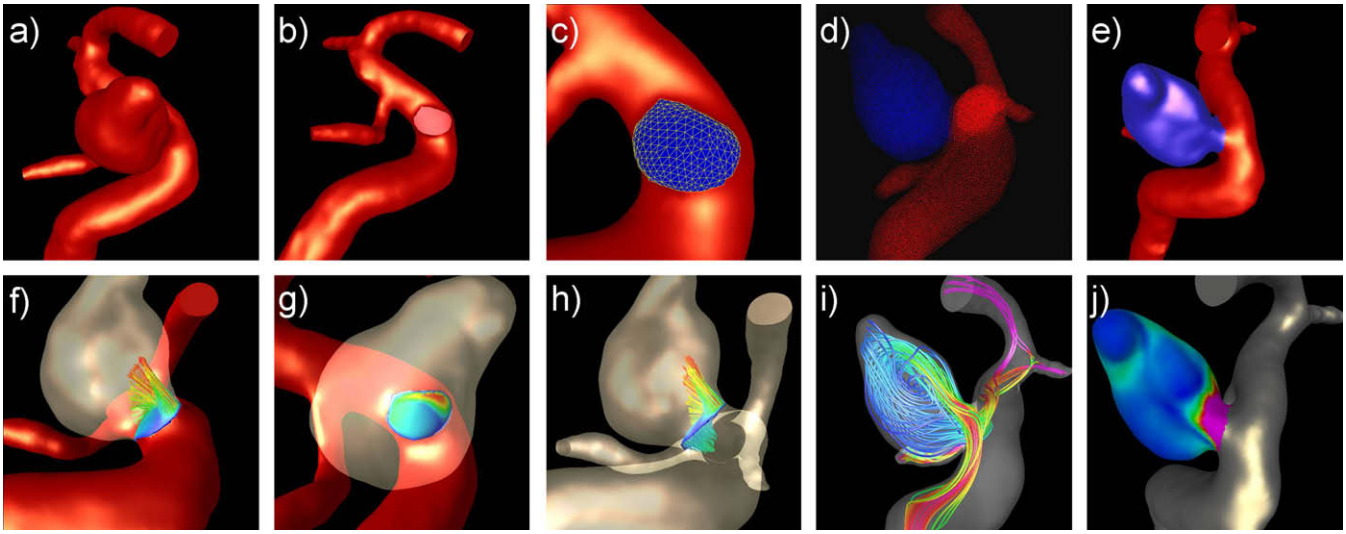

Fig. 1. Methodology for quantification of aneurysmal hemodynamic modification after stenting.

when a Galerkin finite element approximation is done on the advection terms. Therefore, an edge-based upwind finite element approximation is employed to discretize the equations in space [38,39]. The coupled system is solved iteratively using a fractional step scheme with Lower–Upper Symmetric Gauss–Seidel (LU-SGS) relaxation for the advection parts and a preconditioned conjugate gradient solver for the pseudo-Laplacian of the pressure. The scheme has been optimized over many years, and has been detailed elsewhere [33].

2.4.1. Treatment of embedded objects

The edges of the computational grid cut by the surface of the stent, which either represented as a triangulation or as a set of overlapping spheres, are identified. At the intersection points a

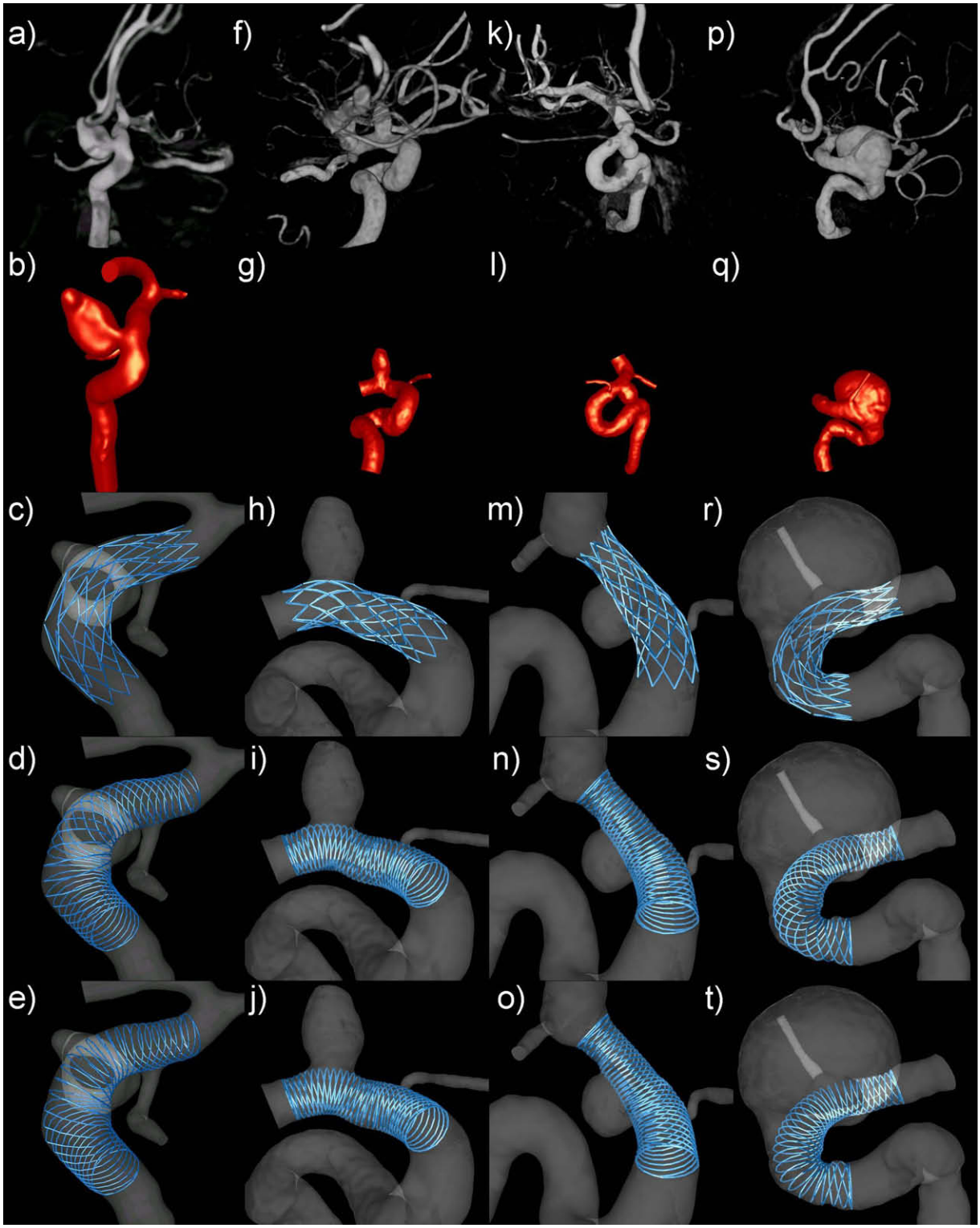

Fig. 2. Original 3DRA images (first row), computational models (second row) and the three stents deployed into the vascular models (third, fourth and fifth rows). Patient 1: a–e; Patient 2: f–j; Patient 3: k–o; Patient 4: p–t.

no-slip boundary condition is automatically introduced and the cut edges are excluded from the flow calculation. In addition, regions of connected edges that lie outside the computational domain, e.g. completely inside the stent wires, are identified and deactivated. An attractive feature of this embedded approach is that it only requires minimal modification of existing incompressible flow solvers. For further details of this technique the reader is referred to [33].

2.4.2. Boundary conditions

To make the simulations simple, vessel walls were assumed rigid in this work. Although in reality there is wall motion which can have a major influence on the hemodynamic variables, sensitivity analyses conducted using vessel deformations measured with dynamic imaging technique show that flow characteristics such as size and location of the flow impaction zone and intra-aneurysmal flow patterns do not change significantly in comparison to simulations conducted using rigid walls [19]. No-slip boundary conditions, $v = 0$, are prescribed at the vessel walls. Pulsatile physiologic flow boundary conditions are used in the simulations. Volumetric flow rate curves measured with phase-contrast magnetic resonance techniques on a number of normal subjects are used to obtain generic flow waveforms for different arteries and scaled to the patient-specific vessel diameter [46]. The inflow velocity distribution is obtained as a superposition of Womersley profiles for each of the Fourier modes of the prescribed flow rate curve [40,41]. The boundary conditions assume fully developed flows and no secondary flows at the inlet boundaries. Previous studies have shown that if subject-specific models are truncated too close to the aneurysm neck fully developed flow conditions can have a significant effect on the intra-aneurysmal hemodynamics [42,43]. However, for anatomical models with longer upstream portions of the parent artery these assumptions have less influence because they allow for the development of

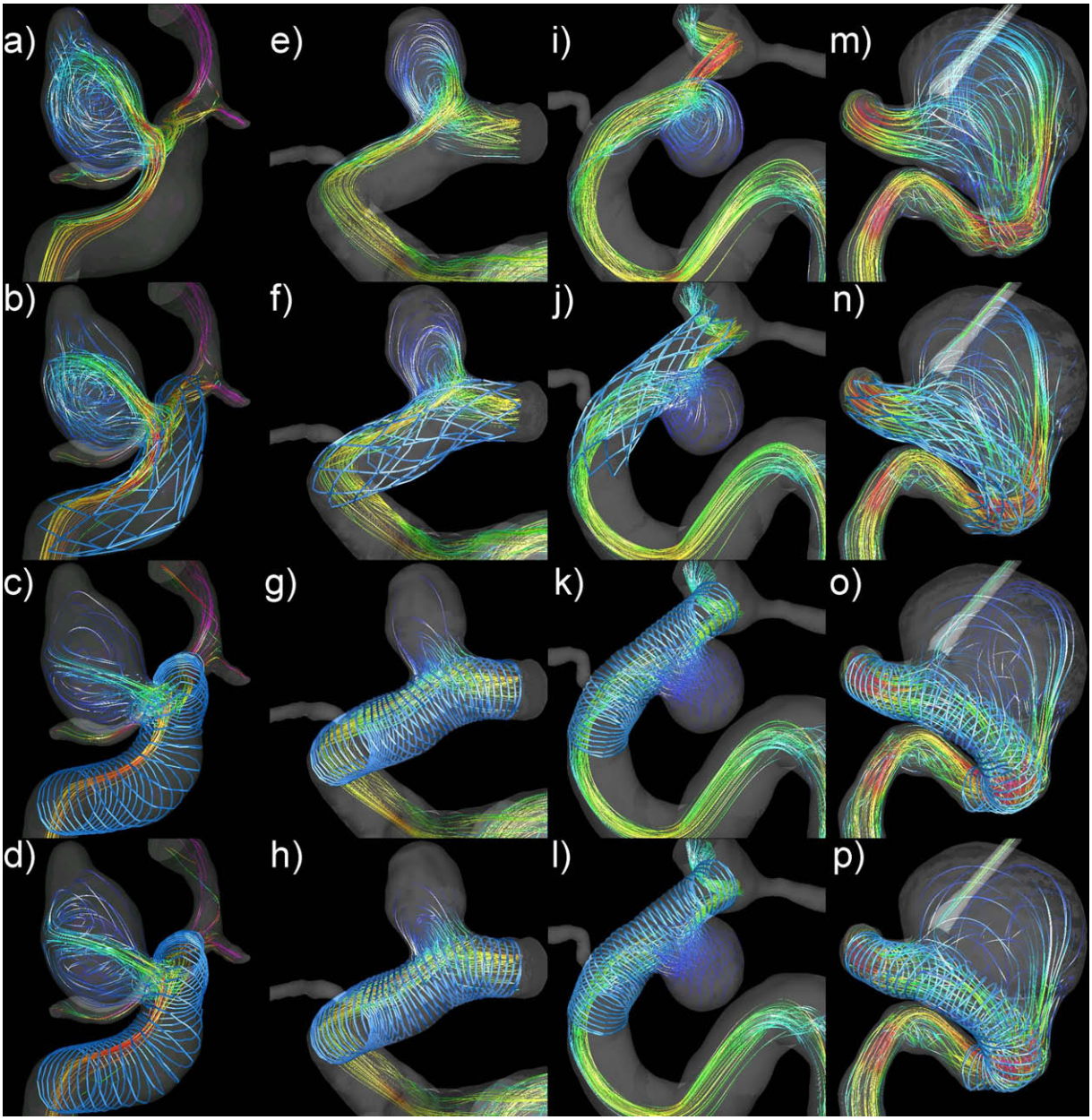

Fig. 3. Streamlines for the four aneurysm models, pre-stented case (top row), with Neuroform stent (second row), left helical stent (third row) and right helical stent (bottom row). Patient 1: a–d; Patient 2: e–h; Patient 3: i–l; Patient 4: m–p.

appropriate secondary flows due to the curvature and tortuosity of the parent vessel. In the present work, the entire upstream portion of the parent artery visible in the anatomical images are included in the models. This typically includes at least one turn of the internal carotid artery which may be enough to produce realistic secondary flows at the location of the aneurysm. Typically, traction-free boundary conditions are imposed at the outflow boundaries. This assumes that the corresponding distal vascular beds have similar flow impedances. More realistic approaches have included imposing impedance boundary conditions from morphometric data [40], modeling the distal vascular bed as a block of porous material [44], or coupling to 1D models of the systemic circulation [45]. In any of these approaches, the values of the vascular bed parameters (flow rate, impedances, porosities, etc.) have to be 'tuned' in order to avoid unrealistic pressure drops or jumps in the wall shear stress in small vessels included in the vascular models.

2.5. Data reduction and visualization

In order to quantify the changes in aneurysmal hemodynamic variables produced by the deployment of a stent the following methodology is used. First the neck of the aneurysm is defined by interactively selecting points along the neck of the aneurysm on the surface mesh. Points along the geodesic path between selected points are identified and selected. The selected points are then deleted from the triangulation, effectively cutting the surface mesh into two pieces, one representing the aneurysm sac and the other the parent artery. The hole in the parent artery mesh representing the neck of the aneurysm is then triangulated. This surface is then used to label the grid points of the volumetric grid lying on each side of the neck surface. For this purpose, the edges cut by the neck surface are identified and an advancing layers algorithm is used to mark the points on each side of this surface. The result of this step is a mask identifying grid points that belong to the

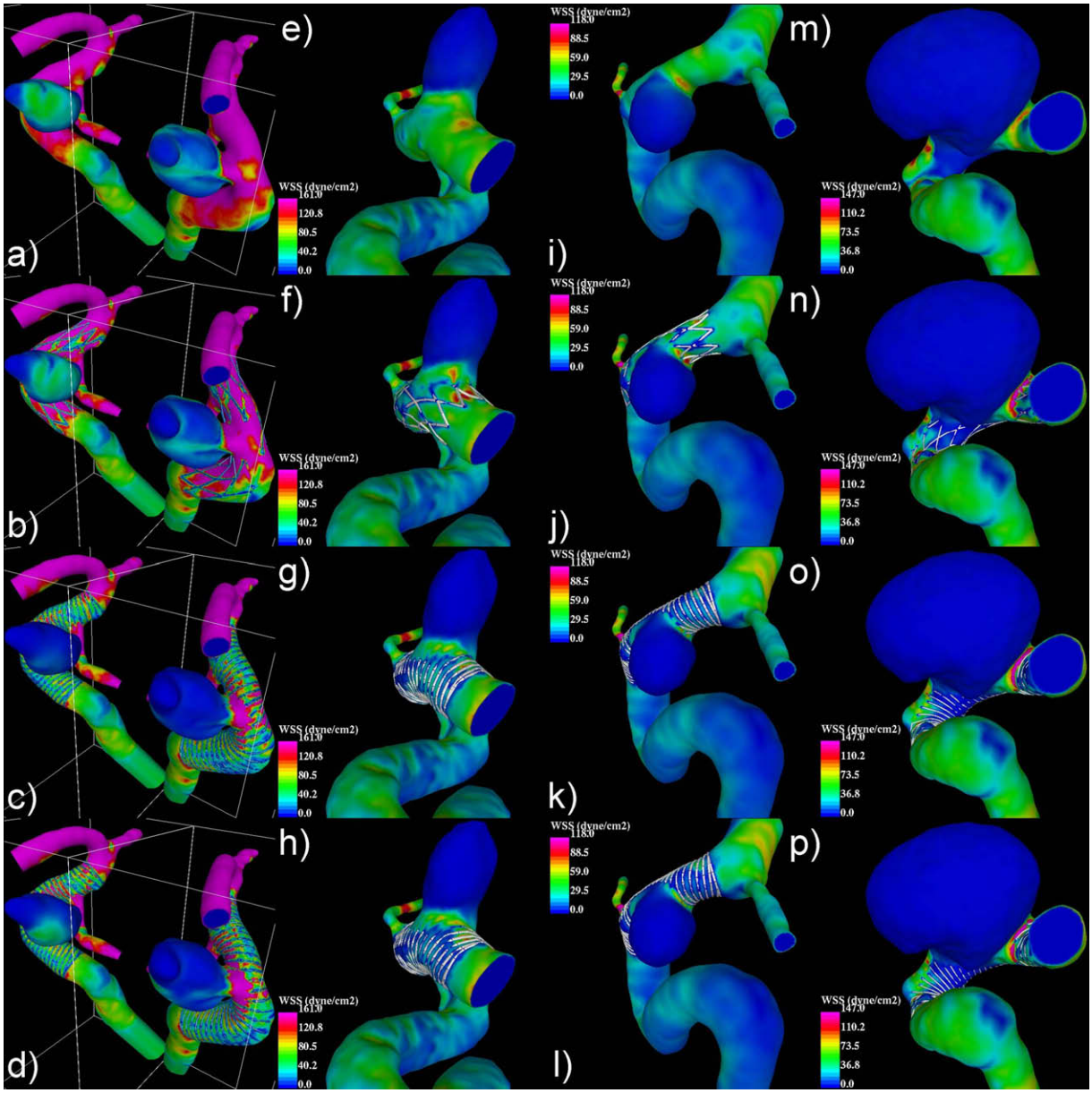

Fig. 4. Wall shear stress for the four aneurysm models, pre-stented case (top row), with Neuroform stent (second row), left helical stent (third row) and right helical stent (bottom row). Patient 1: a–d; Patient 2: e–h; Patient 3: i–l; Patient 4: m–p.

aneurysm or the parent artery. Finally, this mask is used to calculate the minimum, maximum and spatial average of a number of hemodynamic variables in the aneurysm and parent artery regions. The hemodynamic variables considered include: the absolute velocity, the vorticity magnitude, the kinetic energy, the shear rate (second invariant of the shear rate tensor), and wall shear stress magnitude. In addition, flow variables are interpolated from the volumetric grid to the surface triangulation defining the neck. This allows the quantification of hemodynamic variables at the neck such as the total mass flux into the aneurysm.

The labeling of aneurysm and parent artery grid points allows for the visualization of hemodynamic variables in each region separately. Intra-aneurysmal flow patterns are visualized by automatically generating sets of streamlines originating at the center of each of the elements of the aneurysm region and propagated forward and backwards. The aneurysmal inflow pattern is visualized by plotting the velocity profile on the interpolated to the neck surface. These visualizations depict the inflow and outflow regions, the secondary flows at the aneurysm neck, and are useful to determine the size and location of the inflow and outflow portions of the neck.

The methodology is illustrated in Fig. 1. This figure shows the original surface model of an aneurysm in the internal carotid artery (a), the parent artery after removal of the aneurysm sac with a hole at the neck (b), the triangulated neck (c), and the labeling of aneurysm and parent artery points in the volume and surface meshes (d and e). Examples of visualizations of hemodynamic variables are shown in the bottom row of Fig. 1: (f) velocity vectors at the aneurysm neck, (g) velocity magnitude at the aneurysm neck, (h) velocity profile at the aneurysm neck, (i) streamlines through the aneurysm region, and (j) wall shear stress distribution on the aneurysm sac.

3. Results

3.1. Effects of stent design

In this section, the methodology is demonstrated by simulating the effects of three different stent designs on four patient-specific models of internal carotid artery (ICA) aneurysms (a total of 12 simulations). This illustrate how the methodology can be used to select the best available flow diverting device for a given aneurysm. The vascular models were created from 3DRA images as described in the methods section. Volume renderings of the 3DRA images of the aneurysms and the corresponding vascular models with the various stent designs are shown in Fig. 2. The aneurysms were located in the left ICA for patients 1 and 4, and in the right ICA for patients 2 and 3. The first stent design made up of rhomboidal cells corresponds to the Neuroform stent from Boston Scientific Inc. (third row of Fig. 2), and the other two stents are helical stents with the stent wire pointing towards the left (fourth row of Fig. 2) and right directions (fifth row of Fig. 2). The two helical stents had the same pitch angle and porosity, the only difference was their orientation. These idealized helical stents were chosen in order to investigate whether they had different effects on swirling flows rotating in different directions such as in the left and right ICA's. Pulsatile flow calculations were performed without and with the stents inside the vascular models. Visualizations of the flow structures in the aneurysms and parent artery as well as distributions of the wall shear stress (WSS) at peak systole, before and after stenting are presented in Figs. 3 and 4, respectively. Values of hemodynamic variables before and after stenting with each stent are presented in Table 1. This table lists the ratio of the aneurysm inflow to the parent artery flow rate (Q_{in}/Q_0), the maximum and mean velocity in the aneurysm (v_{max} and v_{mean}), the mean vorticity

Table 1
Quantitative values for results shown in Figs. 3 and 4. Stent 1: Neuroform; Stent 2: helix left; Stent 3: helix right.

	Q_{in}/Q_0 (%)	V_{max} (cm/s)	V_{mean} (cm/s)	ω_{mean} (1/s)	$\dot{\gamma}_{mean}$ (1/s)	τ_{max} (dyne/cm^2)	τ_{mean} (dyne/cm^2)
Patient 1							
Pre-stent	14%	181.72	22.91	556.25	414.22	446.76	40.61
Stent 1	16%	161.87	22.21	522.66	391.71	957.96	36.94
	(−13%)	(11%)	(3%)	(6%)	(5%)	(−114%)	(9%)
Stent 2	9%	85.76	7.10	160.18	125.69	286.81	9.83
	(36%)	(53%)	(69%)	(71%)	(70%)	(36%)	(76%)
Stent 3	11%	109.51	10.63	251.27	187.50	323.38	16.78
	(21%)	(40%)	(54%)	(55%)	(55%)	(28%)	(59%)
Patient 2							
Pre-stent	13%	39.90	3.83	86.37	73.89	95.49	5.73
Stent 1	8%	34.78	2.03	45.30	34.21	118.61	3.62
	(38%)	(13%)	(47%)	(48%)	(54%)	(−24%)	(63%)
Stent 2	5%	17.62	1.02	18.80	22.00	81.08	1.80
	(57%)	(56%)	(73%)	(78%)	(70%)	(15%)	(69%)
Stent 3	6%	21.37	1.09	20.82	23.80	68.95	1.90
	(53%)	(46%)	(28%)	(76%)	(68%)	(28%)	(33%)
Patient 3							
Pre-stent	19%	20.00	2.82	71.17	60.51	82.94	5.11
Stent 1	12%	17.07	1.37	33.92	34.08	102.83	2.82
	(38%)	(15%)	(49%)	(52%)	(44%)	(−24%)	(45%)
Stent 2	8%	11.52	0.95	20.51	21.16	95.95	1.98
	(58%)	(42%)	(66%)	(72%)	(65%)	(−16%)	(61%)
Stent 3	8%	9.85	0.93	20.48	20.84	97.40	2.09
	(58%)	(51%)	(33%)	(71%)	(65%)	(−17%)	(59%)
Patient 4							
Pre-stent	91%	53.61	5.40	58.21	44.91	111.08	4.74
Stent 1	80%	49.36	4.03	41.71	34.21	346.29	3.98
	(12%)	(8%)	(25%)	(28%)	(24%)	(−212%)	(16%)
Stent 2	67%	46.41	2.90	25.69	23.29	323.04	2.51
	(26%)	(13%)	(46%)	(56%)	(48%)	(−191%)	(47%)
Stent 3	63%	47.35	2.71	23.88	21.62	297.81	2.42
	(31%)	(12%)	(50%)	(59%)	(52%)	(−168%)	(49%)

(ω_{mean}), the mean shear rate ($\dot{\gamma}_{mean}$) and the maximum and mean wall shear stress magnitude (τ_{max} and τ_{mean}). The percentages in parentheses represent the change in the corresponding hemodynamic variables from before to after stenting (i.e. the modification of the hemodynamic variables caused by stenting). Positive changes mean reduction of the hemodynamic variables while negative changes represent increases.

In the first patient, the inflow jet is located towards the left and distal part of the neck, impacting on the distal part of the body of the aneurysm. All the stents are seen to diffuse the inflow jet and re-direct it towards the dome of the aneurysm, and reduce the WSS in the aneurysm. In this case, the left helical stent produces significant changes in the hemodynamic variables. This stent produces larger reductions in all the hemodynamic variables compared to the other two stents (see Table 1). Comparing this left helical stent with the Neuroform stent the minimum difference in the percentage change in hemodynamic variables was 42% for v_{max} and the maximum difference was 150% for τ_{max}. With respect to the right helical stent the minimum difference was 8% for τ_{max} and maximum difference was 17% for τ_{mean}.

In patient 2, the inflow is located at the distal part of the neck and the intra-aneurysmal flow circulates in counter-clockwise direction (Fig. 3e). The Neuroform stent produces very little modification to the flow pattern (Fig. 3f) but an increase in the WSS at the distal part of the neck can be observed (Fig. 4f). This is because blood is being squeezed between the stent wires and the vessel walls. In contrast, the two helical stents produce more significant flow modifications. In particular, they shift the inflow to the proximal part of the neck and change the direction of the intra-aneurysmal flow circulation to clockwise (Fig. 3g and h). As in the previous case, the left helical stent seems to cause the largest reductions in the hemodynamic variables (see Table 1). Comparing the left helical stent with the Neuroform stent the minimum difference in the percentage change in hemodynamic variables was 6% for τ_{mean} and the maximum difference was 43% for v_{max}. With respect to the right helical stent the minimum difference was -13% for τ_{max} and the maximum difference was 45% for v_{mean}.

In patient 3, the inflow is located in the distal part of the neck and the flow recirculates in the clockwise direction (Fig. 3i). All stents diffuse and deviate the inflow jet towards the left part of the neck. However, they do not change the direction of flow circulation in this aneurysm. In this case all stents produced an increase in the maximum wall shear stress, however a more pronounced increase in the WSS at the distal neck can be observed for the Neuroform stent (Fig. 4j). The helical stents seem to yield smoother flow patterns, i.e. less vortical structures, than the Neuroform (Fig. 3k and l). Again, the stent that seems to cause a larger reduction in the hemodynamic variables is the left helical stent (Table 1). In comparison with the Neuroform stent the minimum difference was 8% for τ_{max} and the maximum difference was 27% for v_{max}. With respect to the right helical stent there was no difference in the percentage change for Q_{in}/Q_0 and $\dot{\gamma}_{mean}$ and the maximum difference was 33% for v_{mean}.

In patient 4, the inflow is located at the proximal part of the neck and flow mainly circulates in the counter-clockwise direction (Fig. 3m). In this case, the Neuroform stent seems to concentrate the inflow jet (Fig. 3n), while the helical stents produce a small diffusion of the inflow jet and a smoother intra-aneurysmal flow pat-

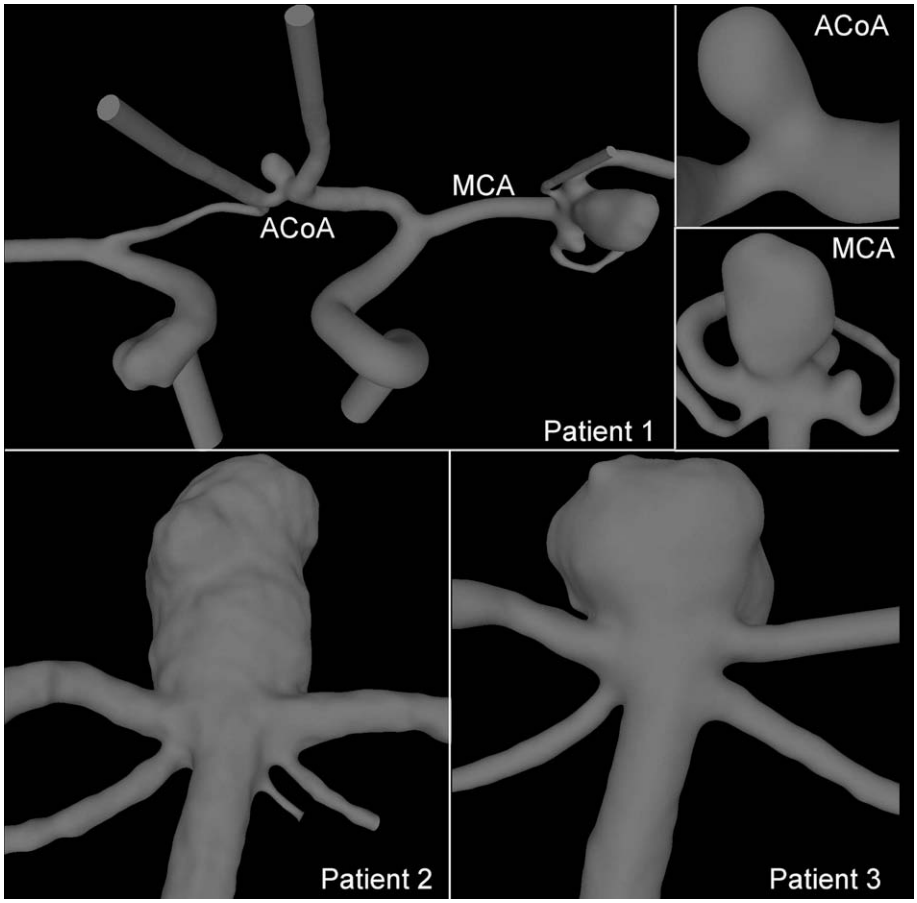

Fig. 5. Patient-specific vascular models of three patients. Model with three aneurysms (top left corner) and their close-up view (top right corner), and two basilar tip aneurysm models (bottom row).

tern (Fig. 3o and p). All stents produced an increase of the WSS at the distal neck, without changing the circulation direction. In this case, the stent that produced the largest reduction in all hemodynamic variables was the right helical stent (see Table 1). Comparing the right helical stent with the Neuroform stent the minimum difference was 4% for v_{max} and the maximum difference was 44% for τ_{max}. With respect to the left helical stent the minimum difference was −1% for v_{max} and maximum difference was 23% for τ_{max}.

3.2. Effects of treatment options

This section illustrates how the methodology can be used to select the best therapeutic option for a given patient. Three patients with intracranial aneurysms are considered. One patient had two aneurysms in the left middle cerebral artery (MCA) and one in the anterior communicating artery (ACoA). The other two patients had wide neck aneurysms at the tip of the basilar artery (BA). Patient-specific models were constructed from 3DRA images. For patient 1, bilateral 3DRA images were used to create the vascular model including the left and right ICA's and MCA's. The anatomical models of these three patients are shown in Fig. 5.

For each aneurysm, different treatment options were considered. Each option consisted in deploying one or two Neuroform stents in different ways. For the ACoA aneurysm of patient 1, the first option was to place a stent from the A1 segment of left anterior cerebral artery (ACA) to the A2 segment of the left ACA. The second option consisted in placing the stent from the left A1 to the right A1. For the MCA aneurysm and for the BA aneurysms of patients 2 and 3 the first option was to place a stent from the parent artery to one of the daughter branches. The second option was to place the stent from the parent artery to the other daughter branch, and the third option was to place two stents from the parent artery to each of the daughter branches (stent in stent technique). A total of six simulations were carried out for this analysis. The flow patterns at peak systole for each aneurysm

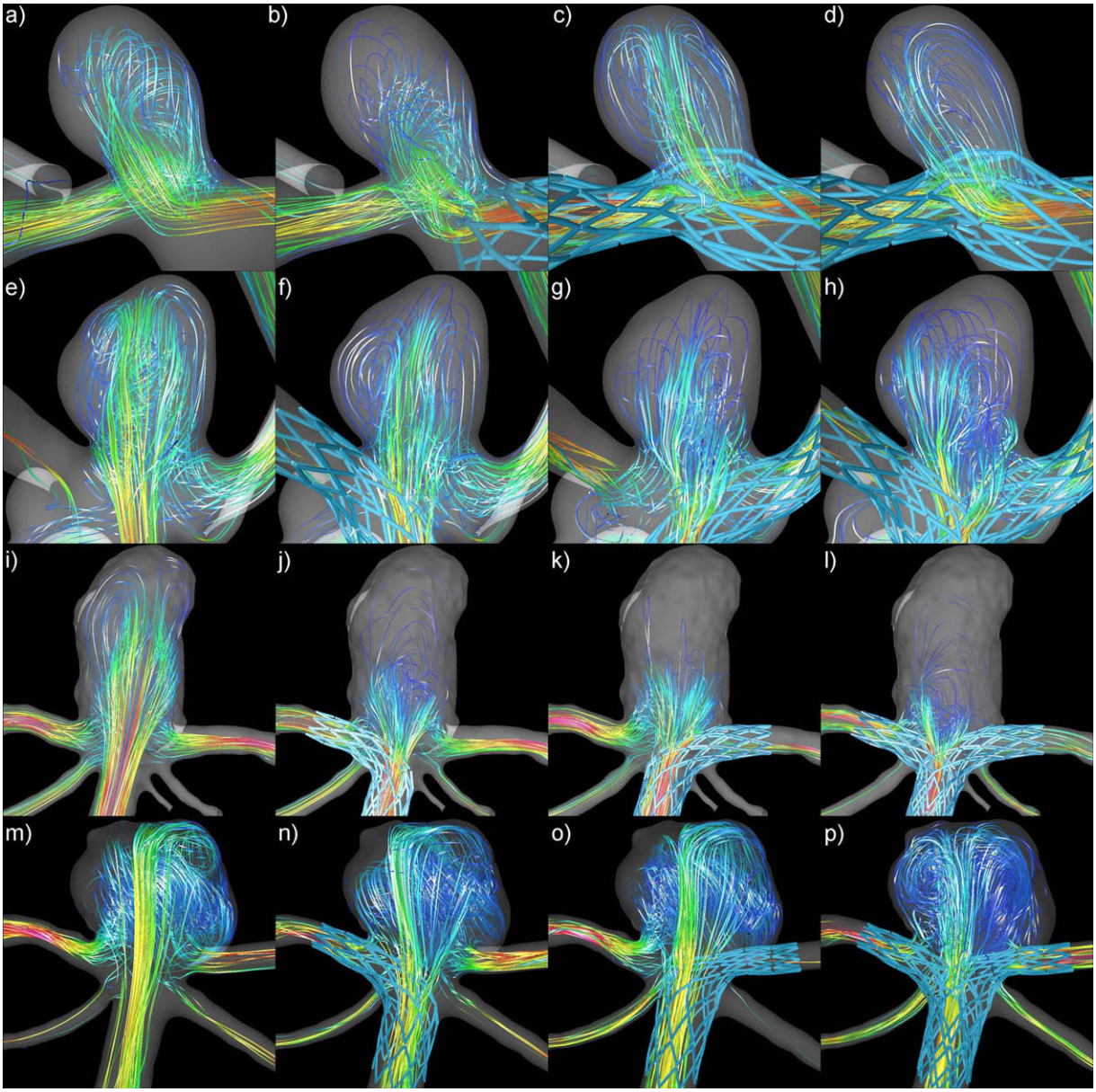

Fig. 6. Streamlines depicting the intra-aneurysmal flow patterns before and after the different treatment options. Patient 1, AcoA aneurysm: a–d; Patient 1, MCA aneurysm: e–h; Patient 2: i–l; Patient 3: m–p.

before stenting and after treatment with each option are presented in Fig. 6. The corresponding distributions of WSS are presented in Fig. 7. The values of hemodynamic variables and their modification produced by each treatment option are listed in Table 2.

The ACoA aneurysm of patient 1 is fed from the left ACA with a fairfly wide inflow jet that impacts on the back wall of the aneurysm producing a relatively high WSS in the body and dome of the aneurysm (Figs. 6a and 7a). When the stent is placed from the left A1 to the left A2, the inflow jet is disrupted causing a significant alteration in the intra-aneurysmal flow pattern and reduction of the WSS (Figs. 6b and 7b). However, there is still a region of elevated WSS at the same impaction zone. When the stent is placed across the neck of the aneurysm (from the left A1 to the right A2) the inflow jet is slightly deviated towards the dome of the aneurysm and the major flow structures within the aneurysm are not significantly modified (Fig. 6c). The region of elevated WSS is found at the dome of the aneurysm (Fig. 7c). A second simulation for of this option was carried out after rotating the stent half a cell. In this case, there is more obstruction of the inflow jet, a less complex velocity pattern, but slightly higher WSS in the aneurysm (Figs. 6d and 7d).

In the MCA aneurysm of patient 1, the inflow jet impacts on the dome of the aneurysm creating a region of elevated WSS along the body and dome of the aneurysm (Figs. 6e and 7e). When deploying the stent from the parent vessel to the left branch, the inflow jet is slightly diffused, the intra-aneurysmal vortical structures are modified, and the WSS is reduced at the dome of the aneurysm (Figs. 6f and 7f). At the same time the inflow into the smaller MCA aneurysm is also reduced. When the stent is deployed to the other daughter (right) branch, there is a larger obstruction of the inflow jet and a more complex intra-aneurysmal flow pattern with an overall lower WSS in the aneurysm (Figs. 6g and 7g). However, the inflow into the smaller MCA aneurysm is increased. When deploying one stent to each of the daughter branches, the intra-aneurysmal flow pattern displays new vortical structures, i.e. more complex flow pattern, and lower WSS in the aneurysm (Figs. 6h

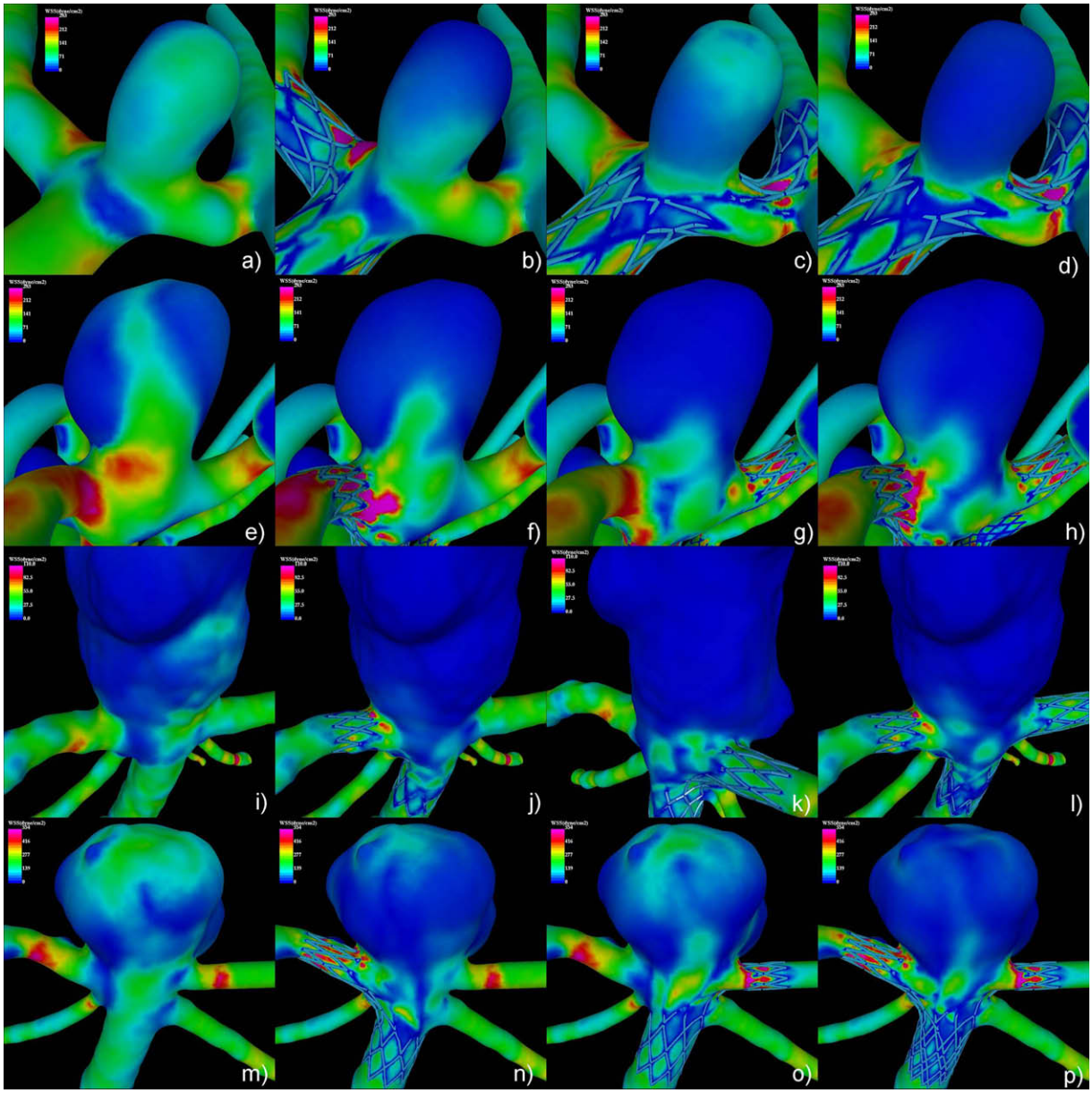

Fig. 7. Wall shear stress distributions before and after the different stenting options. Patient 1, AcoA aneurysm: a–d; Patient 1, MCA aneurysm: e–h; Patient 2: i–l; Patient 3: m–p.

Table 2
Quantitative values for results shown in Figs. 6 and 7.

	Q_{in}/Q_0 (%)	V_{max} (cm/s)	V_{mean} (cm/s)	ω_{mean} (1/s)	$\dot{\gamma}_{mean}$ (1/s)	τ_{max} (dyne/cm^2)	τ_{mean} (dyne/cm^2)
Patient 1 (ACoA)							
Pre-stent	19	86.07	18.53	727.01	547.52	278.64	75.09
LA1 to LA2	12	71.86	10.12	387.68	314.05	530.50	69.39
	(34%)	(17%)	(45%)	(47%)	(43%)	(−90%)	(8%)
LA1 to RA2	12	102.49	14.24	674.52	503.54	644.74	71.24
	(38%)	(−19%)	(23%)	(7%)	(8%)	(−131%)	(5%)
LA1 to RA2 rotated	9	90.43	8.61	390.20	301.56	679.51	71.66
	(55%)	(−5%)	(54%)	(46%)	(45%)	(−144%)	(5%)
Patient 1 (MCA)							
Pre-stent	51	101.67	16.26	415.97	304.74	282.60	71.93
Left	48	80.76	8.98	185.05	152.14	684.02	70.16
	(7%)	(21%)	(45%)	(56%)	(50%)	(−142%)	(2%)
Right	34	48.61	5.51	119.84	104.03	667.19	69.14
	(33%)	(52%)	(66%)	(71%)	(66%)	(−136%)	(4%)
Both	22	52.89	4.37	100.57	87.64	685.53	69.69
	(57%)	(48%)	(71%)	(76%)	(71%)	(−143%)	(3%)
Patient 2							
Pre-stent	84	36.75	4.34	60.77	46.10	109.37	14.07
Left	52	23.25	1.16	16.07	14.16	132.09	11.49
	(39%)	(37%)	(73%)	(74%)	(69%)	(−21%)	(18%)
Right	61	28.32	1.53	21.02	18.09	109.25	9.76
	(28%)	(23%)	(65%)	(65%)	(61%)	(0%)	(31%)
Both	28	20.27	0.38	6.50	6.26	125.17	8.48
	(67%)	(45%)	(91%)	(89%)	(86%)	(−14%)	(40%)
Patient 3							
Pre-stent	84	121.37	29.28	617.55	416.83	535.36	99.26
Left	63	99.14	19.14	382.39	265.40	786.10	88.07
	(25%)	(18%)	(35%)	(38%)	(36%)	(−47%)	(11%)
Right	68	123.33	22.50	454.36	310.44	1047.82	107.68
	(19%)	(2%)	(23%)	(26%)	(26%)	(−96%)	(−8%)
Both	41	100.19	11.67	275.56	200.92	1081.84	98.64
	(59%)	(17%)	(60%)	(55%)	(52%)	(−102%)	(1%)

and 7h). At the same time the inflow into the smaller MCA aneurysm is also reduced. However, in this case there is an increase of WSS in the ouflow part of the neck of the aneurysm.

In the BA tip aneurysm of patient 2, the inflow jet impacts on the body of the aneurysm producing a region of elevated WSS on the right side of the aneurysm and then splits and exits towards the left and right posterior cerebral arteries (PCA) (Figs. 6i and 7i). All stenting options produced significant disruption of the inflow jet, reduction of the intra-aneurysmal velocity, alteration of the flow structure, and reduction of the WSS in the aneurysm (Figs. 6j–l and 7j–l). However, when deploying a single stent from the BA to the left PCA (Fig. 7k) there is only a slight increase of the WSS at the outflow part of the neck compared to the other two cases.

In the BA tip aneurysm of patient 3, a concentrated inflow jet impacts on the dome of the aneurysm producing a region of high WSS at the dome and a complex intra-aneurysmal flow pattern (Figs. 6m and 7m). When stenting from BA artery to the right PCA, the inflow jet is slightly deviated to the right but there is still a region of high WSS at the dome (Figs. 6n and 7n). When stenting from the BA to the left PCA, the inflow jet appears to be more concentrated and impacting on a smaller region of the dome (Figs. 6o and 7o). When two stents are deployed, one into each PCA, the inflow jets is diffused, the intra-aneurysmal flow structures are modified, and the WSS in the dome is significantly reduced (Figs. 6p and 7p). However, in all cases an increase of WSS is observed in the outflow regions of the stented aneurysm neck.

In all the double-stenting simulations, a larger reduction in the hemodynamic variables was observed compared to stenting with just one stent (see Table 2). However, these options typically produced an increase of the maximum WSS in the aneurysm. In both BA tip aneurysms, stenting to the left PCA seem to produce the second largest reduction of the hemodynamic variables (after double-stenting) with a smaller increase of the WSS, and the largest reduction in the mean WSS. In the MCA aneurysm of patient 1, the stenting to the right branch produces the second largest reduction in the hemodynamic variables and the largest reduction of the mean WSS.

3.3. Effects of stent positioning

When a stent is deployed to treat an aneurysm, there is little control on the exact positioning of the stent. However, depending on the design of the stent, positioning can potentially have a significant effect on the hemodynamics of the stented aneurysm. Therefore, it is important to study the sensitivity of the flow diversion characteristics of different stent designs to their positioning. This section presents results of different positioning of the Neuroform stent. The same patient-specific models used to study the effects of different stent designs (Section 3.1) were used. One additional simulation was performed for each model by rotating the stent half a cell, i.e. the maximum angular displacement with respect to the initial positioning. The flow patterns and wall shear stress distributions at peak systole are shown in Fig. 8. Table 3 lists the values of hemodynamic variables obtained with the two stent positions for each of the four patients of Section 3.1.

These results show that the flow modifications obtained with the two positioning of the stent are in good agreement. The largest difference occurred for patient 1 (top row of Fig. 8) where there was a difference in the deviation of the inflow jet and the WSS near the inflow zone of the aneurysm neck. Additionally, in the previous section, a difference in the flow patterns obtained for the ACoA aneurysm after repositioning the stent across the aneurysm neck was observed.

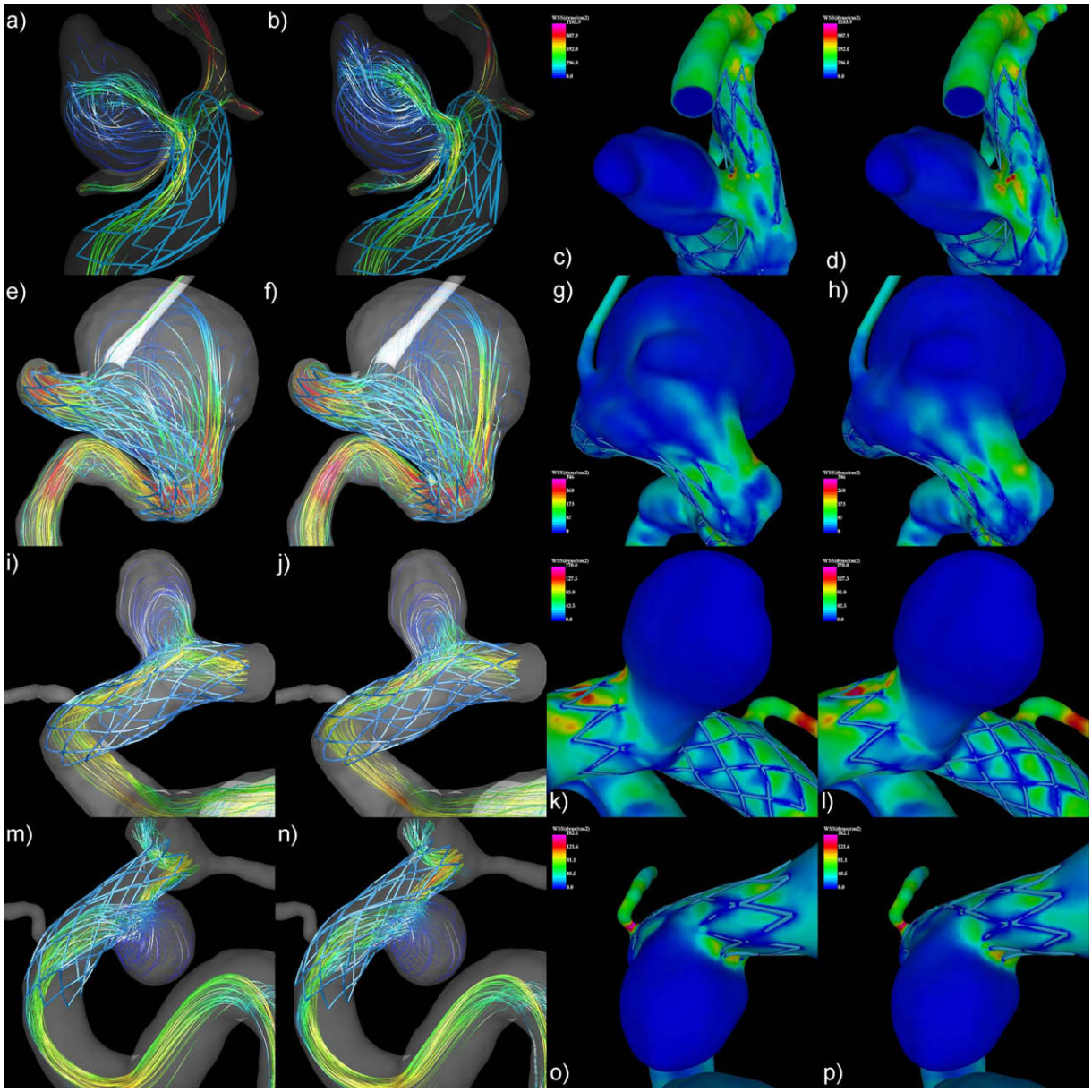

Fig. 8. Streamlines and WSS results for the original stent configuration (first and third column) and the rotated configuration (second and fourth column). Patient 1: a–d; Patient 4: e–h; Patient 2: i–l; Patient 3: m–p.

3.4. Effects of partial stent modeling

When comparing the relative performance of different stents as flow diverters one is often concerned with the alterations of the flow pattern and WSS in the aneurysm and not so much in the detailed flow fields near the walls of the parent vessel. In such cases, the computational expense of the simulations can be significantly reduced if only the portion of the stent that crosses the aneurysm neck is modeled. This would result is much smaller computational meshes. Therefore, in order to assess whether this approach yields reasonable results, comparisons of the flow fields obtained by modeling the entire stent and only the portion that cover the neck were carried out. For this purpose, the same four models of Section 3.1 and the Neuroform stent were used. The original stent models were interactively cut and the portions that lied entirely on the vessel walls were removed. The original and truncated or partial stent models in their deployed state for each patient are shown in Fig. 9.

The results of the flow simulations with both stent models for each patient are presented in Fig. 10. Values of hemodynamic variables obtained with the partial stents are listed in Table 3. These results show that the flow patterns and wall shear stress distributions obtained with the truncated stent models are in good agreement with those obtained with the full stent models. Additionally, the computation times and mesh sizes for the full and truncated stent simulations are presented in Table 4. These results show that a substantial gain in CPU time can be obtained with the truncated models.

4. Discussion

The simulation of flow alteration caused by different endovascular devices has recently gained attention as new flow diverting devices are being designed for treating cerebral aneurysms by themselves. This requires overcoming a number of challenging

Table 3
Quantitative values for results shown in Figs. 8 and 10.

	Q_{in}/Q_0 (%)	V_{max} (cm/s)	V_{mean} (cm/s)	ω_{mean} (1/s)	$\dot{\gamma}_{mean}$ (1/s)	τ_{max} (dyne/cm^2)	τ_{mean} (dyne/cm^2)
Patient 1							
Position 1	16	161.87	22.21	522.66	391.71	957.96	36.94
Position 2	14	194.66	20.75	512.12	392.45	1027.15	40.30
Truncated	15	148.73	20.99	483.89	368.35	935.58	32.96
Patient 2							
Position 1	8	34.78	2.03	45.30	34.21	118.61	3.62
Position 2	8	27.57	1.61	32.94	33.74	94.98	2.76
Truncated	8	34.05	1.96	43.35	40.06	116.54	3.48
Patient 3							
Position 1	12	17.07	1.37	33.92	34.08	102.83	2.82
Position 2	13	18.46	1.53	38.20	37.58	114.07	3.51
Truncated	12	16.69	1.31	32.34	32.70	99.12	2.71
Patient 4							
Position 1	80	49.36	4.03	41.71	34.21	346.29	3.98
Position 2	78	50.18	3.84	40.25	32.92	290.56	3.38
Truncated	74	47.07	3.70	37.93	31.53	336.73	3.53

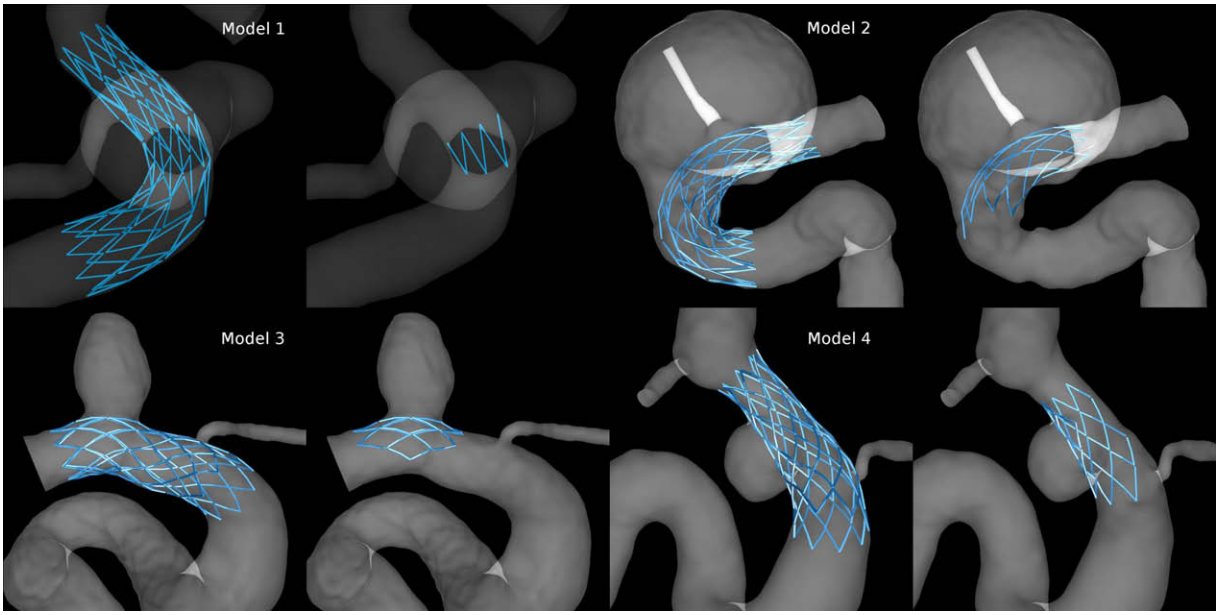

Fig. 9. The full stent and the partial stent for the different aneurysms.

technical problems related to accurate anatomical modeling, deployment of the stents inside patient-specific vascular models, meshing these geometries, computing pulsatile flows around devices realistically and efficiently, comparing the performance of the different stent designs and treatment options, and studying the sensitivity of the calculations with respect to stent positioning and partial modeling. The work presented in this paper represent the first steps towards these aims. In particular, the authors have explored the use of unstructured embedded grids for the personalized modeling of blood flows in stented intracranial aneurysms, have addressed some of the associated technical challenges, and have illustrated the use of the methodology to answer-specific clinical questions.

Currently, a simplistic approach is used to virtually deploy the stent models into the patient-specific vascular models. This approach does not take into consideration the conformability characteristics of the different stents, and neglects any deformation of the parent artery due to the deployment of the stent. Future models need to incorporate these effects for a more accurate representation of the stent geometry in its deployed state.

The unstructured embedded grid approach has been shown to be a powerful technique to deal with complex vascular and device geometries. This strategy allows for the automatic meshing around the endovascular devices in their deployed state. This technique also allows using different representations of the stent geometry (e.g. triangulated surface, overlapping spheres, etc.). Although this approach may tend to produce larger grids than a body-fitted approach to achieve similar resolutions, it is quite easy to use even for geometrically complex situations such as multiple stenting or stent in stent techniques (one stent deployed inside another). Once the vascular model has been constructed and meshed, introducing the stent into grid is straightforward as it only requires an adaptive mesh refinement, which is done automatically in a few minutes. On the other hand, it was shown that modeling only the small portion of the stent that crosses the aneurysm neck is sufficient for studying the intra-aneurysmal hemodynamics while significantly reducing the mesh sizes and computational times. Additionally, previous studies showed that flows past endovascular devices computed with body-fitted and embedded grids were in close agreement [27,28].

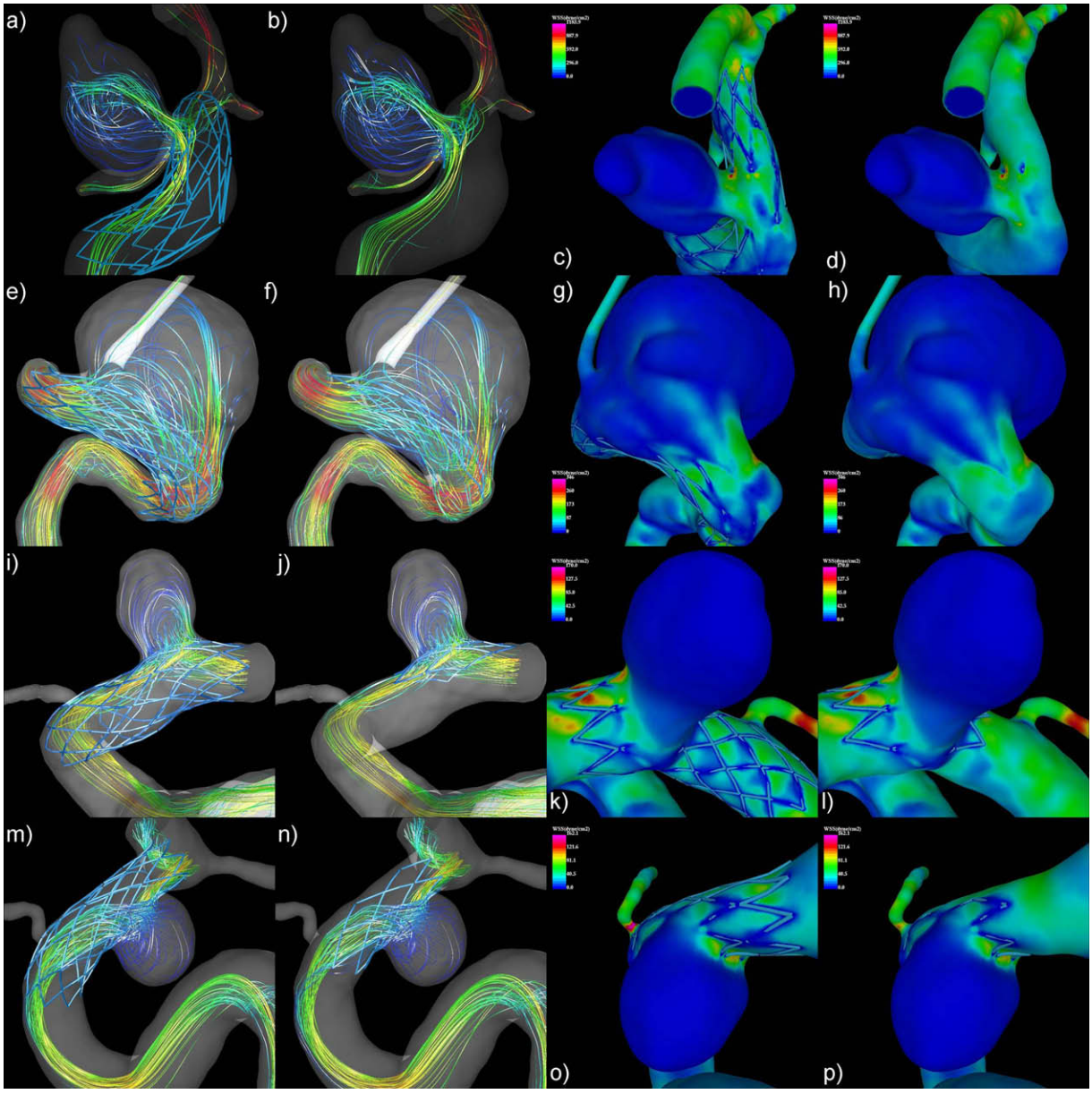

Fig. 10. Streamlines and WSS results for the different aneurysms with full and partial stents. Patient 1: a–d; Patient 4: e–h; Patient 2: i–l; Patient 3: m–p.

The prediction of flow reduction in small arteries branching off from the parent artery near the neck of the aneurysm when a stent is deployed requires appropriate outflow boundary conditions. In these situations (not presented here) the stent may partially cover the origin of these small branches and thus block the flow through them. Clearly, prescribing the flow rate at the outflow boundary would not be realistic as this would assume no change in the flow rate from the pre-stented case. Boundary conditions based on flow impedances or coupling to reduced models of the distal vascular beds seem to be the appropriate choice. However, this requires a proper estimation of the values of the distal impedances, or the parameters of the reduced models, as well as stable methods for imposing these boundary conditions. This is clearly an area that requires further study.

Table 4
Mesh size and computation time taken to simulate flow with the full and partial stents.

	Full		Partial	
	No. of elements (in millions)	Time taken (h)	No. of elements (in millions)	Time taken (h)
Model 1	4.3	20:23	1.25	4:19
Model 2	7.1	16:30	4.8	12
Model 3	5.3	11:43	3	9:17
Model 4	3.9	10	2.3	6:31

The results of virtual stenting four patient-specific aneurysm models with three different stent designs presented here indicate that the same stent can produce different alterations of the hemodynamics of different aneurysms. The flow modifications largely depend on the inflow characteristics of the aneurysm, which in turn depend on the location of the aneurysm and the geometry of the parent vessel. Secondary flows, induced by the turns and tortuosity of the parent artery, play an important role in determining the way in which the flow enters the aneurysm. This could help explain the different dynamical behavior of the two helical stents that have the same geometry except for their direction of rotation.

The increase in WSS observed at the distal neck after stenting is consistent with the results reported by Lieber and Gounis [47], who conducted in vitro, in vivo and numerical experiments to elucidate the effects of different stent design parameters and the prevailing parent vessel hemodynamics on intra-aneurysmal flow patterns. They also observed changes in the circulation direction after stenting of an idealized aneurysm model. However, as shown here these latter observations cannot be generalized to all aneurysms, stent designs and parent artery geometries.

The results presented in this paper illustrated how the methodology can be used not only to select the best available flow diverting device for a given aneurysm but also to select the best therapeutic option. In addition, it was shown that these choices are not always intuitive and should be done on a patient-specific basis, i.e. the best choice for a given patient may not be the optimal choice for another patient. However, this may change with new devices that may be designed to achieve similar flow diversion characteristics in different situations. Additionally, further research is needed in order to develop methods for quantitative evaluation of the performance of different flow diverters. Besides considering fluid dynamical variables such as maximal wall shear stress, total inflow rate, residence times, etc. models that predict the amount of thrombus formation within the aneurysm are required for a more appealing evaluation of the stents and clinical outcomes.

The sensitivity studies presented in this paper indicate that although the positioning of the stent can potentially have a significant effect on the intra-aneurysmal hemodynamics, in many situations these effects are actually quite small. The performance of the stent is related to the number of wires that cross the inflow jet blocking the flow into the aneurysm. This depends not only on the stent design but also on the fluid dynamics characteristics of the aneurysm. It is to expect that the flow diverting characteristics of highly porous stents with asymmetric cell designs will be more dependent on the positioning, especially for aneurysms with thin or concentrated inflow jets. Stents with smaller and symmetrical cells may have more chances of disrupting the inflow jet independently of their positioning.

5. Conclusions

In conclusion, unstructured embedded grids are a viable approach for the patient-specific simulation of endovascular treatment of cerebral aneurysms with flow diverting devices. Although a number of challenges remain to be addressed, it was shown that these models can help design better devices, personalize the endovascular procedures, and answer specific clinical questions.

Acknowledgements

We thank Boston Scientific and Philips Medical Systems for financial support. We also thank Dr. Daniel Rufenacht of the Universite de Geneve for interesting discussions and encouragement.

References

[1] A. Stehbens, Intracranial arterial aneurysms, in: Pathology of the Cerebral Blood Vessels, 1972, pp. 351–470.
[2] F. Linn, G. Rinkel, A. Algra, J. van Gijn, Incidence of subarachnoid hemorrhage: role of region, year, and rate of computed tomography: a meta-analysis, Stroke 27 (4) (1996) 625–629.
[3] G. Foutrakis, H. Yonas, R. Selabassi, Saccular aneurysm formation in curved and bifurcation arteries, Amer. J. Neuroradiol. 20 (1999) 1309–1317.
[4] B. Weir, Unruptured intracranial aneurysms: a revire, J. Neurosurg. 96 (2002) 3–42.
[5] F. Tomasello, D. D'Avella, F. Salpietro, M. Longo, Asumptomatic aneurysms. Literature metanalysis and indications for treatment, J. Neurosurg. 42 (1) (1998) 47–51.
[6] H. Winn, J. Jane, J. Taylor, D. Kaiser, G. Britz, Detection of asymptomatic incidental aneurysms: review of 4568 arteriograms, J. Neurosurg. 96 (1) (2002) 43–49.
[7] M. Kaminogo, M. Yonekura, S. Shibata, Incidence and outcome of multiple intracranial aneurysms in a defined population, Stroke 34 (1) (2003) 16–21.
[8] A. Ringer, D. Lopes, A. Boulos, L. Guterman, L. Hopkins, Current techniques for endovascular treatment of intracranial aneurysms, Semin. Cerebrovasc. Dis. Stroke 1 (1) (2001).
[9] P. Lylyk, A. Ferrario, B. Pasbon, C. Miranda, G. Doroszuk, Buenos Aires experience with the Neuroform self-expanding stent for the treatment of intracranial aneurysms, J. Neurosurg. 102 (2) (2005) 235–241.
[10] K.O. Lövbald, H. Yilmaz, A. Chouiter, D.S.M. Ruiz, G. Abdo, P. Bijlenga, N. Tribolet, D.A. Rüfenacht, Intracranial aneurysm stenting: follow-up with MR angiography, J. Magn. Reson. Imag. 24 (2006) 418–422.
[11] I. Szikora, Z. Berentei, Z. Kulcsar, K. Barath, A. Berez, A. Bose, I. Nyary, Endovascular treatment of intracranial aneurysms with parent vessel reconstruction using balloon and self expandable stents, Acta Neurochir. 148 (2006) 711–723.
[12] M. Ohta, S.G. Wetzel, P. Dantan, C. Bachelet, K.O. Lovbald, H. Yilmaz, P. Flaud, D.A. Rüfenacht, Rheological changes after stenting of a cerebral aneurysm: a finite element modeling approach, Cardiovasc Intervention. Radiol. 28 (2005) 768–772.
[13] S.C.M. Yu, J.B. Zhao, A steady flow analysis on the stented and non-stented sidewall aneurysm models, Med. Engrg. Phys. 21 (1999) 133–141.
[14] A.K. Wakhloo, B.B. Leiber, Alteration of hemodynamics in aneurysm models by stenting: influence of stent porosity, Ann. Biomed. Engrg. 25 (1997) 460–469.
[15] K. Barath, F. Cassot, J.H. Fasel, Influence of stent properties on the alteration of cerebral intra-aneurysmal hemodynamics: flow quantification in elastic sidewall aneurysm models, Neurol. Res. 27 (2005) 120–128.
[16] L.D. Jou, C.M. Quick, W.L. Young, M.T. Lawton, R. Higashida, A. Martin, D. Saloner, Computational approach to quantify hemodynamic forces in giant cerebral aneurysms, Amer. J. Neuroradiol. 24 (9) (2004) 1804–1810.
[17] D. Steinman, J. Milner, C. Norley, S. Lownie, D. Holdworth, Image-based computational simulation of flow dynamics in a giant intracranial aneurysm, Amer. J. Neuroradiol. 24 (4) (2003) 559–566.
[18] J.R. Cebral, M. Hernandez, A.F. Frangi, Computational analysis of blood flow dynamics in cerebral aneurysms from CTA and 3D rotational angiography image data, in: ICCB03, Zaragoza, Spain, September, 2003.
[19] J.R. Cebral, M. Hernandez, A.F. Frangi, C.M. Putman, M. Pergolizzi, J.E. Burgess, Subject-specific modeling of intracranial aneurysms, in: SPIE Medical Imaging 2004, San Diego, California, February 2004.
[20] J.R. Cebral, M.A. Castro, S. Appanaboyina, C.M. Putman, D. Millan, A.F. Frangi, Efficient pipeline for image-based patient-specific analysis of cerebral aneurysm hemodynamics: technique and sensitivity, IEEE Trans. Med. Imag. 24 (2005) 457–467.
[21] P.J. Ymi, B. Vasbinder, V. Ho, P.L. Choyke, Isosurfaces as deformable models for magnetic resonance angiography, IEEE Trans. Med. Imag. 22 (2003) 875–881.
[22] G. Taubin, A signal processing approach to fair surface design, Comput. Graphics (1995) 351–358.
[23] K. Perktold, G. Rappitsch, Computer Simulation of Arterial Blood Flow, Vessel Diseases Under the Aspect of Local Hemodynamics, Biological Flows Plenum Press, 1995, pp. 83–114.
[24] J.R. Cebral, M.A. Castro, J.E. Burgess, C.M. Putman, Cerebral aneurysm hemodynamics modeling from 3D rotational angiography, in: ISBI 2004, Arlington, Virginia, April 2004.
[25] A.G. Radaelli, L. Augsburger, J.R. Cebral, M. Ohta, D.A. Rfenacht, R. Balossino, G. Benndorf, D.R. Hose, A. Marzo, R. Metcalfe, P. Mortier, F. Mut, P. Reymond, L. Socci, B. Verhegghe, A.F. Frangi, Reproducibility of haemodynamical simulations in a subject-specific stented aneurysm model – a report on the Virtual Intracranial Stenting Challenge 2007, J. Biomech. 41 (10) (2008) 2069–2081.
[26] M. Kim, E.I. Levy, H. Meng, L.N. Hopkins, Quantification of hemodynamic changes induced by virtual placement of multiple stents across a wide-necked basilar trunk aneurysm, Neurosurgery 61 (6) (2007) 1305–1312.
[27] R. Löhner, S. Appanaboyina, J.R. Cebral, Comparison of body-fitted, embedded and immersed solutions of low Reynolds-number 3-D incompressible flows, Int. J. Numer. Methods Fluids 57 (1) (2007) 13–30.
[28] S. Appanaboyina, F. Mut, R. Löhner, C.M. Putman, J.R. Cebral, Computational fluid dynamics of stented intracranial aneurysms using adaptive embedded unstructured grids, Int. J. Numer. Methods Fluids 57 (2008) 475–493.
[29] M. Ohta, C. He, T. Nakayama, A. Takahashi, D.A. Rüfenacht, Three-dimensional reconstruction of a cerebral stent using micro-CT for computational simulation, J. Intell. Mater. Syst. Struct. (2007), doi:10.1177/1045389X07083184.
[30] J.R. Cebral, R. Lohner, S. Appanaboyina, C.M. Putman, Image-based computational hemodynamics methods and their application for the analysis of blood flow past endovascular devices, in: C.T. Leondes (Ed.), Biomechanical Systems Technology: (1) Computational Methods, vol. 1, World Scientific, 2007, pp. 29–85 (Chapter 2).
[31] D. Sforza, C.M. Putman, J.R. Cebral, Hemodynamics of Cerebral Aneurysms, Ann. Rev. Fluid Mech. 41 (2009) 91–107.
[32] R. Löhner, J. Baum, E. Mestreau, D. Sharov, Adaptive embedded unstructured grid methods, Int. J. Numer. Methods 60 (2003) 641–660.
[33] J.R. Cebral, R. Löhner, Efficient simulation of blood flow past complex endovascular devices using an adaptive embedding technique, IEEE Trans. Med. Imag. (2005). special issue on Vascular Imaging.

[34] T.R. Hughes, The Finite Element Method: Linear Static and Dynamic Finite Element Analysis, Dover Publications, 2000.
[35] R. Löhner, Regridding surface triangulations, J. Comput. Phys. 126 (1996) 1–10.
[36] R. Löhner, Automatic unstructured grid generators, Finite Elem. Anal. Des. (1997) 111–134.
[37] J. Mazumdar, Biofluid Mechanics, World Scientific, 1992.
[38] R. Löhner, Applied CFD Techniques, John Wiley & Sons, 2001.
[39] R. Löhner, C. Yang, J.R. Cebral, O. Soto, F. Camelli, J. Waltz, Improving the speed and accuracy of projection-type incompressible flow solvers, AIAA-03-3991-CP, 2003.
[40] C. Taylor, T. Hughes, R. Löhner, O. Soto, P. Choyke, Finite element modeling of blood flow in arteries, Comput. Methods Appl. Mech. Engrg. 158 (1998) 155–196.
[41] J.R. Cebral, P. Yim, R. Löhner, O. Soto, P. Choyke, Blood flow modeling in carotid arteries using computational fluid dynamics and magnetic resonance imaging, Acad. Radiol. 9 (2002) 1286–1299.
[42] M.A. Castro, C.M. Putman, J.R. Cebral, Computational fluid dynamics modeling of intracranial aneurysms: effects of parent artery segmentation on intraaneurysmal hemodynamics, Amer. J. Neuroradiol. (2006) 27 1703–1709.
[43] J.R. Cebral, R. Löhner, Flow visualization on unstructured grids using geometrical cuts, vortes and shock surfaces, AIAA-2001-915, 2001.
[44] A. Ferrandez, T. David, J. Bamford, J. Scott, A. Guthrie, Computational models of blood flow in the circle of Willis, Comput. Methods Biomech. Biomed. Engrg. 4 (1) (2000) 1–26.
[45] L. Formaggia, D. Lamponi, M. Tuveri, A. Veneziani, Numerical modeling of 1D arterial networks coupled with a lumped parameters description of the heart, Comput. Methods Biomech. Biomed. Engrg. 9 (5) (2006) 273–288.
[46] J.R. Cebral, M.A. Castro, O. Soto, R. Löhner, N. Alperin, Blood-flow models of the circle of willis from magnetic resonance data, J. Engrg. Math. 47 (2003) 369–386.
[47] B.B. Lieber, M.J. Gounis, The physics of endoluminal stenting in the treatment of cerebrovascular aneurysms, Neurol. Res. 24 (1) (2002) S33–S42.